



Published in final edited form as:

Cell Rep. 2021 October 19; 37(3): 109848. doi:10.1016/j.celrep.2021.109848.

Lysosomal Zn²⁺ release triggers rapid, mitochondria-mediated, non-apoptotic cell death in metastatic melanoma

Wanlu Du^{1,2,*}, Mingxue Gu^{1,2}, Meiqin Hu¹, Prateeksunder Pinchi¹, Wei Chen¹, Michael Ryan¹, Timothy Nold¹, Ahmed Bannaga¹, Haoxing Xu¹

¹Department of Molecular, Cellular, and Developmental Biology, University of Michigan, 4104 Biological Sciences Building, 1105 North University Ave., Ann Arbor, MI 48109, USA

SUMMARY

During tumor progression, lysosome function is often maladaptively upregulated to match the high energy demand required for cancer cell hyper-proliferation and invasion. Here, we report that mucolipin TRP channel 1 (TRPML1), a lysosomal Ca²⁺ and Zn²⁺ release channel that regulates multiple aspects of lysosome function, is dramatically upregulated in metastatic melanoma cells compared with normal cells. TRPML-specific synthetic agonists (ML-SAs) are sufficient to induce rapid (within hours) lysosomal Zn²⁺-dependent necrotic cell death in metastatic melanoma cells while completely sparing normal cells. ML-SA-caused mitochondria swelling and dysfunction lead to cellular ATP depletion. While pharmacological inhibition or genetic silencing of TRPML1 in metastatic melanoma cells prevents such cell death, overexpression of TRPML1 in normal cells confers ML-SA vulnerability. In the melanoma mouse models, ML-SAs exhibit potent *in vivo* efficacy of suppressing tumor progression. Hence, targeting maladaptively upregulated lysosome machinery can selectively eradicate metastatic tumor cells *in vitro* and *in vivo*.

Graphical Abstract

This is an open access article under the CC BY-NC-ND license (<http://creativecommons.org/licenses/by-nc-nd/4.0/>).

*Correspondence: wanludu@umich.edu.

AUTHOR CONTRIBUTIONS

Conceptualization, W.D.; methodology, W.D. and M.G.; investigation, W.D., M.G., M.H., P.P., W.C., M.R., T.N., and A.B.; writing, W.D., M.G., and H.X.; supervision, W.D. and H.X.; funding acquisition, W.D. and H.X. All authors reviewed and proofread the manuscript.

²These authors contributed equally

SUPPLEMENTAL INFORMATION

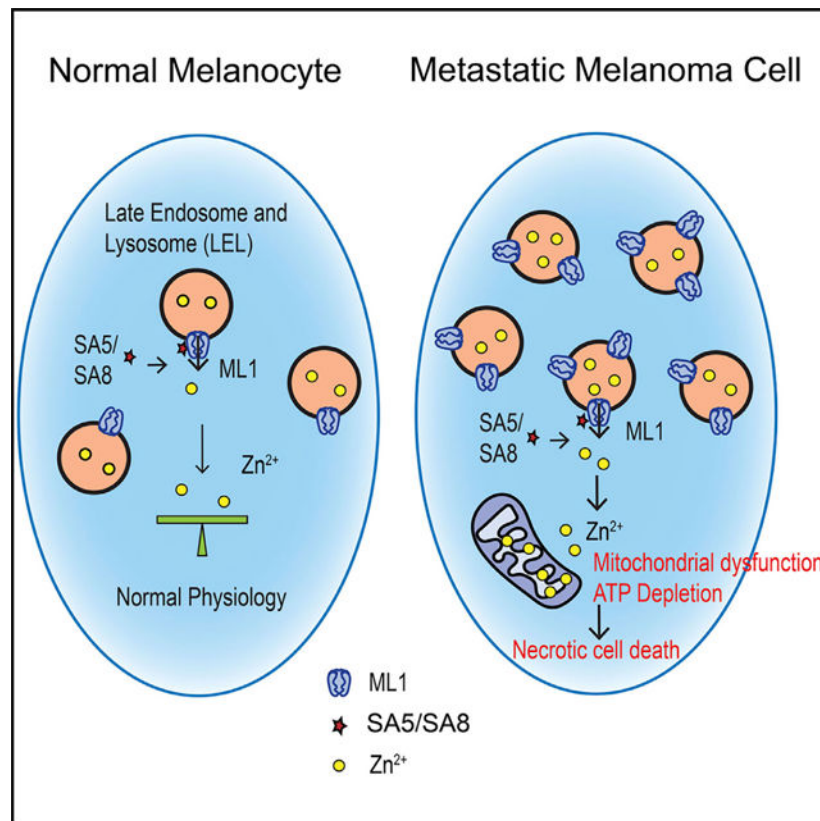
Supplemental information can be found online at <https://doi.org/10.1016/j.celrep.2021.109848>.

DECLARATION OF INTERESTS

H.X. is the scientific cofounder and partial owner of CalyGene Biotechnology, Inc. and Lysoway Therapeutics, Inc. and an inventor of the US Provisional Patent Application No. 62/894,289. All other authors declare no competing interests.

INCLUSION AND DIVERSITY

One or more of the authors of this paper self-identifies as an underrepresented ethnic minority in science. One or more of the authors of this paper received support from a program designed to increase minority representation in science.



In brief

Du et al. show that lysosomal TRPML1 is dramatically upregulated in metastatic melanoma cells and can be targeted by small molecules, TRPML1-specific synthetic agonists (ML-SAs). ML-SAs show potent and selective cytotoxicity in melanoma cells while sparing normal cells. Additionally, ML-SAs exhibit potent *in vivo* efficacy by suppressing tumor progression.

INTRODUCTION

Once metastasized, melanoma skin cancer responds poorly to the traditional anti-cancer options, calling for a need to develop novel treatment strategies (Narayana et al., 2013; Welsh et al., 2016). Lysosomes, the cellular hub in metabolism, protein degradation, and nutrient sensing, play an indispensable role in cell survival and growth in normal physiology (Lawrence and Zoncu, 2019). In the metastatic cancer, lysosomes are often “transformed” to be hypertrophic (Katheder et al., 2017; Kroemer and Jäättelä, 2005), actively contributing to tumor progression, not only in cancer cell proliferation and survival by providing nutrients via macromolecule degradation but also in cancer invasion and metastasis by secreting lysosomal hydrolases to digest the extracellular matrix (Finicle et al., 2018; Hämälistö and Jäättelä, 2016). Due to a high energy demand of cancer cells, the function of lysosomes is often adaptively or maladaptively upregulated to meet the metabolic requirement of cancer cells (Kallunki et al., 2013; Piao and Amaravadi, 2016). Given the heavy dependence on lysosome machinery for hyper-proliferation and invasion, cancer cells are particularly

sensitive to lysosome disruptions (Serrano-Puebla and Boya, 2018). Lysosome inhibitors and/or inducers of lysosome membrane permeability are reportedly effective in triggering cancer cell death (McAfee et al., 2012; Petersen et al., 2013; Tardy et al., 2006). However, broad-spectrum lysosome inhibition, such as inhibitors of vacuolar type ATPase (v-ATPase), may inevitably compromise the functions of normal cells and tissues (Pérez-Sayáns et al., 2009). Hence, it is more desirable to target specific lysosomal machineries that operate in normal physiology but are maladaptively upregulated in cancer.

Mucolipin TRP channel 1 (TRPML1/MCOLN1; ML1) is a Ca^{2+} and $\text{Zn}^{2+}/\text{Fe}^{2+}$ dually permeable cation channel predominantly localized on the membranes of late endosomes and lysosomes (LELs) in all mammalian cell types (Cheng et al., 2010; Dong et al., 2008). The related ML2 and ML3 channels are also permeable to Ca^{2+} , as well as heavy metal ions, but are more restrictively expressed (Cheng et al., 2010; Li et al., 2019). Using TRPML-specific synthetic agonists (ML-SAs) and synthetic inhibitors (ML-SIs), which bind directly to TRPML proteins in the atomic-resolution co-structures (Schmiege et al., 2017; Schmiege et al., 2021), we and others have demonstrated that TRPML channels, especially ML1, play essential roles in various lysosomal functions, which include lysosome movement, membrane trafficking, lysosomal exocytosis, lysosome biogenesis, and heavy metal homeostasis (Dong et al., 2008; Li et al., 2016; Minckley et al., 2019; Peng et al., 2020; Samie et al., 2013; Yu et al., 2020).

While a high level of ML1 expression may serve as a favorable prognostic marker for several types of cancer, RNA sequencing (RNA-seq) analysis revealed that the highest expression among them is in melanoma (WebLink, 2019). Although several recent loss-of-function studies suggest that ML1 inhibition or knock down could reduce cancer cell proliferation, the effects were marginal even over time courses of days (Jung et al., 2019; Shekoufeh Almasi et al., 2020; Xu et al., 2019). Whereas no gross growth phenotype is seen in *Trpml1* knockout (KO) mice and type IV mucopolindosis patients (Venugopal et al., 2007), the Genome-wide Cancer Dependence Map showed that ML1 is dispensable for cancer cell survival (DepMap, <https://depmaporg/portal/gene/MCOLN1?tab=overview>). Consistent with these observations, we found that prolonged inhibition of ML1 using ML-SIs that are much more potent than the published ones barely inhibited the growth of multiple cancer cell lines (unpublished data). In the current study, we found that small-molecule activation, but not inhibition of ML1, induced selective cell death of metastatic melanoma *in vitro* and *in vivo*.

RESULTS

Lysosomal ML1 channels are upregulated in metastatic melanoma cells

We examined the protein expression levels of ML1 in normal skin tissues, nevus (benign), and metastatic melanoma using immunohistochemistry with a ML1-specific antibody (Sahoo et al., 2017). Much stronger immunoreactivities were seen in the metastatic melanoma tissues compared with normal skin and benign nevus (Figures 1A and 1B). Consistently, in two highly metastatic melanoma cell lines, MeWo and M12, which have been intensively studied for their high metastatic capabilities *in vitro* and *in vivo* (Du et al., 2017; Pietrobono et al., 2020; Shiku et al., 1976; Xie et al., 1997), quantitative

real-time PCR and western blotting analyses revealed 2-to-4-fold increases in the mRNA and protein expression levels of ML1 compared with normal, non-cancerous immortalized human melanocytes (Figures S1A–S1C).

To compare the channel activities of lysosomal ML1 in the cells, we performed patch-clamp recordings on chemically enlarged LELs (Dong et al., 2008) isolated from normal melanocytes, MeWo, and M12 cells. Whole-endolysosome ML1-mediated currents (I_{ML1}) were activated by ML-SAs (Figures 1C–1E), which included ML-SA1 (Shen et al., 2012) and the more potent ML-SA5 and ML-SA8 (Sahoo et al., 2017; Yu et al., 2020) (potency SA1 < SA5 < SA8; Figure S1E), and inhibited by ML-SI3 and ML-SI4 (Sahoo et al., 2017; Yu et al., 2020) (Figure S1F). Note that the specificities of ML-SAs and ML-SIs have been previously validated using ML1 KO cells (Sahoo et al., 2017; Shen et al., 2012; Yu et al., 2020; Zhang et al., 2016) and confirmed in the atomic-resolution co-structures (Schmiege et al., 2017; Schmiege et al., 2021). Remarkably, whole-endolysosome I_{ML1} was 30-to-75-fold larger in MeWo and M12 cells compared with normal melanocytes (Figure 1F). It is possible that in the metastatic melanoma cells, additional posttranslational mechanisms, e.g., increased lysosomal delivery of ML1 and accessory factors, may contribute to the much more dramatic upregulation in the lysosomal currents, relative to the mild increases in the total mRNA and protein expression levels.

Considering the established role of ML1 in activating transcription factor EB (TFEB), a master regulator of lysosome biogenesis (Li et al., 2019; Medina et al., 2015; Napolitano and Ballabio, 2016), we studied whether other lysosomal machineries were also upregulated in the metastatic melanoma cells. The protein expression level of lysosome-associated membrane protein 1 (LAMP1), a commonly used lysosomal marker (Saftig and Klumperman, 2009), was also increased by more than 2 folds in both MeWo and M12 cells compared with normal melanocytes (Figures S1B and S1D). In addition, the fluorescent intensity of LysoTracker, a marker for lysosomal acidification (Tasdemir et al., 2008), was also increased (Figure S1G). It is worth noting that LAMP1 expression is reportedly elevated in aggressive brain tumors (Jensen et al., 2013). Taken together, these results suggest that lysosomal ML1 channels, or likely lysosome biogenesis in general, were upregulated in metastatic melanoma cells.

Selective cytotoxicity of ML-SAs to metastatic melanoma cells

We next investigated the roles of ML1 upregulation in the growth and survival of metastatic melanoma cells. No significant effects of ML-SI3 or ML-SI4 (0.1–100 μ M for 12 h) on M12 or MeWo cell viability, measured by the cellular ATP level with the CellTiter-Glo ATP assay, were observed (Figure S2A). In contrast, both ML-SA5 and ML-SA8 induced substantial cell death in M12 and MeWo cells while completely sparing normal melanocytes (Figures 2A–2C and S2B). Within 0.5 to 2 h, ML-SA-treated MeWo and M12 cells exhibited cell round-up and swelling, which are morphological changes characteristic of necrotic cell death (Kroemer et al., 2009) (Figure S2B; Videos S1 and S2), followed by reduced cell viability (Figures 2B, 2C, and 2H) and loss of membrane integrity as detected by propidium iodide (PI) staining (Figures 2D, 2E, and S2B). ML-SA-induced cell death occurred in a dose- (Figures 2B, 2C, 2F, and 2G) and time-dependent manner (Figure S2B).

In the PI staining assay used for the further cytotoxicity analyses, we set the treatment dose to 3 μM and 1 μM for ML-SA5 and ML-SA8, respectively, and the treatment time to 3 h and 6 h for M12 and MeWo cells, respectively. Notably, the cytotoxic effects of ML-SAs were completely blocked by a co-treatment of ML-SI3 or ML-SI4 (Figures 2I–2K and S2C), indicating the on-target specificity of ML-SA5/8 in the cell-death assays. ML-SA1, which was much less potent than ML-SA5 or ML-SA8 in the channel assays (Figures S1E and S1F), had only weak cytotoxic effects in the high concentrations ($>50 \mu\text{M}$) (data not shown), so ML-SA1 was not studied further in the cell-death assays. In a sharp contrast, non-cancerous human melanocytes displayed no obvious vulnerability to ML-SA treatment (Figures 2A, 2D, 2E, 2H, and S2B). In addition, ML-SA-induced cytotoxicity was not observed in HEK293 cells, human fibroblasts, or two commonly used cancer cell lines: HeLa and SH-SY5Y (Figures 2H and S2D). On the other hand, significant but slightly weaker cytotoxicity was seen in MDA231-BrM2, a human breast-to-brain metastatic cancer cell line (Bos et al., 2009) (Figure 2H). Put together, these results suggest that ML-SAs selectively induce rapid, necrosis-like cell death in metastatic melanoma cells and possibly in other metastatic cancer cells as well.

ML-SA-induced cytotoxicity is dependent on the expression level of ML1

We next studied whether ML1 is required for ML-SA-induced cell death of metastatic melanoma cells by silencing the expression of ML1 using RNA interference (Kukic et al., 2013). In the siML1-transfected, ML1 knocking-down MeWo and M12 cells, in which whole-endolysosome I_{ML1} was reduced by more than 80% (Figure 3A), ML-SA-induced cell death was significantly decreased (Figures 3B–3D), indicating that ML1 is required for ML-SA cytotoxicity in the metastatic melanoma cells. Note that knock down efficiency and genetic compensation (e.g., ML2/3 channels) might have contributed to the residual ML-SA cytotoxicity in the siML1-transfected cells.

We also investigated whether increasing the expression of ML1 in ML-SA-insensitive cells is sufficient to confer ML-SA vulnerability. Since HEK293 is not sensitive to ML-SA treatment (Figure S2D), we performed the test in the ML1-overexpressing HEK293 cells. In the Tet-On-HEK293-GCaMP7-ML1 stable cells (Zhang et al., 2019), in which ML1 expression was induced by doxycycline (Dox), cells became vulnerable to ML-SAs upon Dox application (Figure 3E). Likewise, HEK293 cells that were transiently transfected with EGFP-ML1 (HEK ML1 OE) also became sensitive to ML-SA treatment, and the vulnerability was diminished by ML-SIs (Figures 3F, 3G, S2E, and S2F). Hence, ML1 upregulation may have played an essential role in ML-SA cytotoxicity in metastatic melanoma cells.

ML-SA-induced cell death is a Zn^{2+} -dependent process

Lysosomal ML1 is a non-selective cation channel that is permeable to Ca^{2+} , as well as heavy metal ions such as Fe^{2+} and Zn^{2+} (Dong et al., 2008). Give the well-established role of Ca^{2+} in cell death (Orrenius and Nicotera, 1994), we first examined whether Ca^{2+} is required for ML-SAs' cytotoxicity in M12 and MeWo cells. Surprisingly, BAPTA-AM, a membrane-permeable Ca^{2+} chelator (Garrity et al., 2016) that readily blocked ML-SA-evoked lysosomal Ca^{2+} release and TFEB nuclear translocation (Figures S3A and

S3B), failed to prevent ML-SA's cytotoxicity in metastatic melanoma cells (Figures 4A–4D). Likewise, EGTA-AM, another Ca^{2+} chelator, was also without effect (Figure S3C). Furthermore, cyclosporin A (CsA), a calcineurin inhibitor that reportedly blocks ML-SA-induced Ca^{2+} -dependent TFEB nuclear translocation (Medina et al., 2015), or knocking down TFEB expression also failed to prevent ML-SA-induced cell death (Figures S3D and S3E). Hence, the well-documented ML1- Ca^{2+} -TFEB pathway (Li et al., 2019; Napolitano and Ballabio, 2016) might not play a dominant role in ML-SA-induced cell death.

In contrast, N,N,N,N-Tetrakis(2-pyridylmethyl)-ethylenediamine (TPEN), a membrane-permeable, relatively specific, high-affinity Zn^{2+} chelator (Radford and Lippard, 2013) (Figure S4A), which exhibited no inhibitory effect on lysosomal Ca^{2+} release or TFEB nuclear translocation (Figures S3A and S3B), completely prevented ML-SA-induced cytotoxicity in M12 and MeWo cells (Figures 4A–4D, S4B, and S4C). Likewise, 1,10-phenanthroline (1,10-PT), another zinc chelator (Yang et al., 2007) (Figure S4A), also significantly reduced ML-SA-induced melanoma cell death (Figure S4D). In the ML1-overexpressing HEK293 cells, TPEN, but not BAPTA-AM, diminished ML-SA's cytotoxicity (Figures 4E, 4G, S4E, and S4F). Considering that ML1 is a Zn^{2+} -permeable channel (Figure S4G), the collective results suggest that ML1's Zn^{2+} permeability, but not its Ca^{2+} permeability, underlies ML-SA's cytotoxicity.

Activation of ML1 releases lysosomal Zn^{2+} to cause cell death in metastatic melanoma cells

Lysosomes are vesicular Zn^{2+} stores and a major source for the free Zn^{2+} pool in the cytoplasm (Haase and Beyersmann, 1999; Palmiter et al., 1996). A link between ML1 and lysosomal Zn^{2+} release has been recently established (Cuajungco et al., 2014; Minckley et al., 2019); in ML1-deficient cells, cellular Zn^{2+} is reportedly accumulated in the lysosomes (Eichelsdoerfer et al., 2010; Kukic et al., 2013). We hypothesize that ML-SA's cytotoxicity is attributed to lysosomal Zn^{2+} release upon ML1 activation. FluoZin-3-AM, a cell membrane-permeable Zn^{2+} -sensitive fluorescent dye ($K_d = 15$ nM), can be used to monitor not only cytoplasmic [Zn^{2+}] but also vesicular [Zn^{2+}], due to its relative insensitivity to acidic pH (Devinney et al., 2005) (Figure S4H). In MeWo and M12 cells, the strongest FluoZin-3 signal was detected in the vesicular compartments that were LysoTracker-positive (Figure 4H), suggesting that lysosomes are the major intracellular Zn^{2+} stores in MeWo and M12 cells. Notably, ML-SA5 significantly decreased vesicular FluoZin-3 fluorescence in M12 cells (Figures 4I and 4J). In the HEK293 and MeWo cells that were transfected with ML1 tagged with GZnP3 (genetically encoded Zn^{2+} indicator, GZnP3-ML1), but not in the cells that were transfected with GZnP3-Rab7 (Minckley et al., 2019), ML-SA induced increases in the cytoplasmic GZnP3 signal (Figures 4K and 4L). Taken together, these data suggest that ML-SAs activate lysosomal ML1 to induce Zn^{2+} release from lysosomal Zn^{2+} stores.

In the MeWo and M12 cells that were incubated with extracellular Zn^{2+} , vesicular Zn^{2+} levels were found to be elevated (Figure 4M). In these cells, ML-SA5-induced cytotoxicity was synergistically increased (Figure 4N), suggesting that ML1 activation causes cell death via Zn^{2+} release from lysosomes in metastatic melanoma cells

ML-SAs induced mitochondrial swelling and dysfunction

To explore the cell death mechanism(s) underlying ML-SA's cytotoxicity, we tested a panel of established inhibitors for various cell death pathways, which included necrostatin-1 (Nec-1) for necroptosis (Degterev et al., 2005), pan-caspase inhibitor z-VAD-fmk for apoptosis (Cain et al., 1996), iron chelator deferoxamine (DFO) for ferroptosis (Dixon et al., 2012), and bafilomycin A1 (Baf-A1) and chloroquine (CQ) for autophagic cell death (Tasdemir et al., 2008). None of the tested cell-death inhibitors prevented ML-SA-induced cytotoxicity (Figures S5A–S5E), suggesting that ML-SAs induce a cell-death mechanism distinct from apoptosis, necroptosis, ferroptosis, or autophagic cell death.

Cytosolic Zn^{2+} overload is known to cause mitochondrial damage (Dineley et al., 2003; Sheline et al., 2000), which in turn may cause a rapid drop in cellular ATP levels, as was observed in ML-SA-treated MeWo and M12 cells (Figures 2B and 2C). MitoTracker staining (Gao et al., 2001) revealed that in MeWo and M12 cells, but not in normal melanocytes, mitochondria became swollen and fragmented within 0.5 to 1 hour post ML-SA treatment (Figures 5A–5C). Such morphological changes of mitochondria were not seen in cells that were co-treated with ML-SIs or TPEN (Figures 5D and 5E). Extensive mitochondrial swelling was also evident in the ML-SA-treated cells under the transmission electron microscopy (TEM) examination (Figures 5F and 5G). Tetramethylrhodamine methyl ester (TMRM) staining revealed that ML-SA5 treatment also caused a loss of mitochondrial membrane potential in M12 cells (Figure S6). Collectively, these results suggest that ML-SAs caused mitochondrial damage and cellular ATP depletion via ML1 activation and subsequent lysosomal Zn^{2+} release.

ML-SAs inhibit tumor progression in advanced melanoma mouse models

To evaluate the therapeutic efficacy of ML-SAs *in vivo*, we engineered MeWo and M12 cells stably expressing both the fluorescent protein mCherry and the bioluminescent protein firefly luciferase (Fluc) (Du et al., 2017). The modified MeWo and M12 cells, referred to as MeWo-FmC and M12-FmC cells, exhibit similar cell morphology, proliferation, migration, and ML-SA sensitivity compared to the unmodified parental cells (data not shown). In a subcutaneous xenograft melanoma mouse model, *in vivo* bioluminescence imaging was performed weekly to monitor tumor growth. In MeWo-FmC-bearing mice that were randomly separated into vehicle versus ML-SA5-treated groups, intraperitoneal (i.p.) injection of ML-SA5 (5 mg/kg three times per week with drug administration starting one week post-tumor cell inoculation) resulted in a substantial reduction in tumor growth *in vivo* (Figures 6A–6C) without causing obvious systemic toxicity (Figure 6D). Meanwhile, i.p. injection of ML-SA5 (three times per week) into subcutaneous-tumor-bearing mice significantly prolonged animal survival post-tumor implantation (Figure S7).

Since M12 cells are primary melanoma cells derived from melanoma brain metastases (MBM) patients, we created a mouse model of MBM by implanting M12-FmC cells into mouse brain. In mice bearing MBM, single intracranial administration of ML-SA8 (10 mM/5 μ L) was sufficient to markedly suppress MBM cell growth with a survival benefit (Figures 6E–6G). Collectively, our results have demonstrated that pharmacological

activation of ML1 using small-molecule agonists can mitigate metastatic melanoma progression *in vivo*.

DISCUSSION

We have demonstrated in the current study that in metastatic melanoma cells, the maladaptively upregulated lysosomal ML1 channels can be pharmacologically targeted to induce a distinctive form of necrotic cell death by triggering lysosomal Zn^{2+} release to cause mitochondrial swelling/damage and rapid cellular ATP depletion (Figure 7). In contrast to ML-SA-induced cell death that occurs rapidly (within hours) in metastatic melanoma cells, ML1 inhibition was previously reported to exhibit a slow (in days) anti-proliferation effect in cancer cells (Jung et al., 2019; Shekoufeh Almasi et al., 2020; Xu et al., 2019). Whereas under physiological conditions, ML1-mediated lysosomal Zn^{2+} release is required for cellular homeostasis (Kukic et al., 2013), excessive activation of this pathway in metastatic cancer cells, such as MeWo, M12, and MDA-231-BrM2 cells, may induce such cell death (Figure 7). Hence, lysosomal ML1 channels are maladaptively upregulated in metastatic cancer cells, and this maladaptation, as a prognostic marker for advanced melanoma patients, can be targeted for selective eradication of metastatic melanoma cells without affecting normal cells.

Upon certain pathological challenges, such as in stroke and neurodegenerative disorders, increases in cytoplasmic chelatable Zn^{2+} reportedly cause massive neuronal cell death (Koh et al., 1996). Unlike the cytosol, which keeps the free Zn^{2+} concentration as low as 0.1 nM by multiple efflux and buffering mechanisms, intracellular vesicles such as lysosomes contain micromolar to millimolar concentrations of Zn^{2+} , functioning as vesicular Zn^{2+} stores (Blaby-Haas and Merchant, 2014; Minckley et al., 2019; Palmiter et al., 1996). Cancer cells, due to their high metabolism and fast turnover of metal-binding macromolecules, tend to accumulate heavy metal ions in endolysosomal compartments (Chandler et al., 2016; Kroemer and Jäätelä, 2005; Pavlova and Thompson, 2016). Although cytosolic Zn^{2+} , as an essential trace element, is required for normal cellular functions, excessive Zn^{2+} release from intracellular Zn^{2+} stores reportedly inhibits mitochondrial functions, e.g., the electron transport chain, to cause cellular energy failure and subsequent cell death (Sheline et al., 2000). Although our results strongly suggest lysosomal Zn^{2+} as the driving force in ML-SA-caused cell death, the possible contribution of Ca^{2+} to the Zn^{2+} -dominant process cannot be excluded, as ML-SA application evokes lysosomal Ca^{2+} release as well (Figure S3A) (Shen et al., 2012; Yu et al., 2020).

Mitochondria have been implicated in several cell-death pathways, including apoptosis and ferroptosis (Gao et al., 2019). During ferroptosis, mitochondria become condensed and dysfunctional (Dixon et al., 2012). Remarkably distinct features, such as rapid (<1 h) mitochondrial swelling and fragmentation, occur during ML-SA-induced cell death. Although a causative role of mitochondrial swelling/damage in such cell death requires further investigation, the fast time course of mitochondrial swelling suggests that it is the cause of cellular ATP depletion and cell death. How lysosomal Zn^{2+} release causes mitochondrial swelling and damage is not known. A recent study reported that Ca^{2+} is transferred directly from lysosomes into mitochondria upon ML1 activation (Peng et

al., 2020). It is likely that upon ML1 activation, lysosomal Zn^{2+} may also rapidly flux into mitochondria through lysosome-mitochondria membrane contact sites. We hypothesize that certain Zn^{2+} -dependent enzymes or Zn^{2+} regulated mitochondrial membrane proteins may function as the key mediators of ML-SA-induced cell death. For instance, inhibition of crucial enzymes in the ATP synthesis process, e.g., glyceraldehyde 3-phosphate dehydrogenase (GAPDH), by Zn^{2+} may become significant when the free cytosolic or mitochondrial $[Zn^{2+}]$ is elevated (Beyersmann and Haase, 2001; Maret et al., 1999). Hence, Zn^{2+} release channels and transporters such as ML1 (Eichelsdoerfer et al., 2010; Kukic et al., 2013) must be tightly regulated within cells. ML1 upregulation might provide some growth advantage for metastatic cancer cells. However, this upregulation may render these ML1-upregulated cells a unique susceptibility to ML-SAs via the lysosome-initiated, mitochondria-mediated, necrotic cell death. Therefore, pharmacological activation of ML1 may serve as a potential therapeutic strategy for metastatic melanoma or other cancers, in which ML1 upregulation is a prognostic marker.

STAR★METHODS

RESOURCE AVAILABILITY

Lead contact—Further information and requests for resources and reagents should be directed to and will be fulfilled by the Lead Contact, Wanlu Du (wanludu@umich.edu).

Materials availability—All unique/stable reagents generated in this study are available from the Lead Contact with a completed Materials Transfer Agreement.

Data and code availability

- All data reported in this paper will be shared by the lead contact upon request.
- This paper does not report original code.
- Any additional information required to reanalyze the data reported in this paper is available from the lead contact upon request.

EXPERIMENTAL MODEL AND SUBJECT DETAILS

Animal models—Athymic nude mice (females, 8 weeks old, Charles River Laboratories, Wilmington, MA) were used in this study. Mice were housed in standard cages at 21°C with a 12h light-12h dark cycle with access to food (standard laboratory chow) and water *ad libitum*. Based on pilot studies, with a power of 0.8 and $p < 0.05$, we calculated a sample size of between 5 and 11 mice per group. Mice were anesthetized using 2% isoflurane (inhale). For the subcutaneous (*s.c.*) tumor model, MeWo-FmC cells ($1\sim 1.5\times 10^6$ tumor cells/mouse) were suspended in 100 μ L PBS and *s.c.* injected into immunocompromised nude mice. ML-SA5 (dissolved in 10% DMSO, 40% PEG300, and 50% PBS) (Yu et al., 2020) was administered to mice (5 mg/Kg) by intraperitoneal (*i.p.*) injection 3 times a week until the end of experiments. Mice with one of the following conditions: 1) a tumor diameter measuring greater than 2 cm in any single dimension, 2) impairment in the normal movement, 3) ulceration that is greater than 1/2 the surface of the tumor area or has effusions, 4) infection, and 5) hemorrhage, were euthanized according to the Tumor

Burden Policy for Rodents. For the MBM tumor model, M12-FmC cells were implanted stereotactically into nude mouse brains (0.5×10^5 tumor cells/mouse) in the following co-ordinates: 2.2 mm lateral from bregma, 2.5 mm ventral from dura on the cranial suture. ML-SA8 (10 mM/5 μ l) was administered on-site by a single intracranial injection. Mice were imaged for the success of tumor cell injection post-implantation and then periodically for tumor progression using *in vivo* bioluminescent imaging as described previously (Du et al., 2017). During tumor growth, we closely monitored the animal situation and strictly followed the Tumor Burden Policy for Rodents and the End-Stage Illness Scoring System for euthanizing the mice that reached a score of 6–11. All *in vivo* procedures were approved by animal protocol following the Institutional Animal Care Guidelines at the University of Michigan.

Cell culture—The pMEL/NRAS (Q61R) immortalized human melanocytes were cultured in Ham's F-10 Nutrient Mix with 10% fetal bovine serum (FBS) and 1% penicillin-streptomycin. The patient-derived melanoma brain metastatic cells, M12 and MeWo, as well as HEK293, MDA231BrM2, HeLa, and SH-SY5Y cell lines, were cultured in Dulbecco's Modified Eagle Medium supplemented with 10% FBS and 1% penicillin-streptomycin. Human fibroblasts were cultured in Minimum Essential Media supplemented with 10% FBS and 1% penicillin-streptomycin. All cells were used at low passages with occasional testing for mycoplasma contamination by MycoAlert™ Mycoplasma Detection Kit.

METHOD DETAILS

Whole-endolysosome and whole-cell patch-clamp electrophysiology—Whole-endolysosome patch-clamp experiments were performed in isolated enlarged endolysosomes as described previously (Dong et al., 2008; Zhang et al., 2019). Briefly, cells were treated with 1 μ M vacuolin-1 overnight to selectively enlarge the size of late endosomes and lysosomes (LELs). A glass electrode was then used to break the plasma membrane to release the enlarged vacuoles. After formation of a giga-seal between the patch pipette and an enlarged endolysosome, voltage steps of several hundred millivolts with a millisecond duration were applied to break into the vacuolar membrane. All bath solutions were applied via a fast perfusion system that produced a complete solution exchange within a few seconds. Unless otherwise indicated, the bath (cytoplasmic) solution contained (in mM): 140 K-gluconate, 4 NaCl, 1 EGTA, 2 MgCl₂, 0.39 CaCl₂, and 20 HEPES (pH 7.2 adjusted with KOH; free [Ca²⁺]_i approximately equal to 100 nM). The pipette (luminal) solution contained (in mM): 145 NaCl, 5 KCl, 2 CaCl₂, 1 MgCl₂, 10 glucose, 10 HEPES, and 10 MES (pH 4.6 adjusted with NaOH). For whole-cell patch clamp recordings, the pipette (cytosolic) solution contained (in mM): 145 NaCl, 5 KCl, 2 CaCl₂, 1 MgCl₂, 10 glucose, and 10 HEPES (pH 7.4 adjusted with NaOH). The bath (extracellular) solution contained (in mM): 30 ZnCl₂, 110 NaCl, 10 HEPES, and 10 MES (pH 4.6 adjusted with HCl). Glass electrodes were pulled with resistance of 2–4 m Ω (whole-cell) or 9–11 m Ω (whole-endolysosome). Data were collected using an Axopatch 200B amplifier equipped with a Digidata 1440 controlled by Clampex 10.7 software. All experiments were conducted at room temperature (22°C–25°C), and all recordings were analyzed with Clampfit 10.7 and Origin 2018 software.

RNA extraction and RT-qPCR—Total RNA was extracted from the cultured cells using E.Z.N.A.® total RNA kit. The cDNA was then synthesized using a Superscript III RT kit. PCR mixture was prepared with Power-Up SYBR green 2X master mix using the following primers: *GAPDH*, forward (fw): 5'-tgcac caccaactgcttagc-3', reverse: 5'-ggcatggactgtggctcatgag-3'; *MCOLN1*, fw: 5'-gagtgggtgcgacaagtctc-3', rev: 5'-tggtctctcccgaatgac-3'. Real time quantitative PCR was performed with the ABI StepOnePlus RealTime PCR System.

Western blotting—Cells were lysed with ice-cold RIPA buffer in the presence of 1X protease inhibitor cocktail and phosphatase inhibitor cocktail 2, NaF (1 mM), and Na₃VO₄ (1 mM). Protein samples (10–100 µg) were then loaded and separated on 4% to 12% gradient sodium dodecyl sulfate (SDS) polyacrylamide electrophoresis gels and transferred to polyvinylidene difluoride membranes. The membranes were blocked with 1% bovine serum albumin (BSA) or 5% milk in PBS supplemented with 0.1% Tween20 for 1 h and then incubated with primary antibodies against ML1, LAMP1, and β-actin. Bound antibodies were detected with horseradish peroxidase-conjugated anti-rabbit or anti-mouse secondary antibodies and enhanced chemiluminescence reagents. Protein levels were quantified using the ImageJ (NIH) software.

Immunohistochemistry (IHC)—Human paraffin-embedded tissue array (Tissue Microarray, TMA) contained multiple benign tumor (nevus) and metastatic melanoma specimens. Immunohistochemical staining was performed at the University of Michigan Rogel Cancer Center Histology core on the DAKO Autostainer (Agilent, Carpinteria, CA) using Envision Flex+ and diaminobenzadine (DAB) as the chromogen. De-paraffinized sections were labeled with anti-TRPML1 specific antibody at 1:250 for 30 mins at room temperature. Heat induced epitope retrieval using Dako Envision Flex TRS, Low pH was used prior to staining. Appropriate negative (no primary antibody) and positive controls (Titer TMA 4A) were stained in parallel with each set of slides studied. Images were obtained by Nikon's Eclipse E800 microscope.

In vitro cell death assay—Cell death was analyzed by either propidium iodide (PI) staining or CellTiter-Glo® Luminescent Cell Viability Assay. For PI staining, cells were washed twice with cold PBS before being incubated with 10 µg/mL PI for 10 min. Images were acquired with Canon fluorescence microscope and analyzed using ImageJ. For CellTiter-Glo® luminescent cell viability assay, cells (0.5~1 × 10⁴/well) were seeded in 96-well plates and incubated with various chemicals for indicated time periods. Cell viability was measured by a quantitative luminescence assays using an ATP-dependent luminescent reagent according to the manufacturer's instruction manual.

Silencing RNA knockdown—*ML1* and *TFEB* siRNA knockdown were achieved with esiRNA human MCOLN1 (esiRNA1) or stealth siRNA human TFEB transfections by Lipofectamine 2000. The efficiency of the siRNA knockdown was assayed by western blotting or qPCR. Cells were then subjected to electrophysiological and cell biological analyses 72 hours after transfection.

Expression of ML1 in HEK293 cells—GCaMP7-ML1 expression was induced in Tet-On HEK293-GCaMP7-ML1 cells (Zhang et al., 2019) 24h prior to experiments by adding 0.01 $\mu\text{g}/\text{mL}$ doxycycline (Dox). For HEK ML1 OE cells, transient transfection of EGFP-ML1 was performed in HEK293 cells using Lipofectamine 2000.

FluoZin-3, LysoTracker, and MitoTracker Imaging—Fluorescence and time-lapse imaging was conducted in a spinning-disk confocal imaging system composed of an Olympus IX81 inverted microscope, 10 \times , 20 \times , and 60 \times Olympus objectives, a CSU-X1 scanner (Yokogawa), an iXon EM-CCD camera (Andor), a temperature controller, and MetaMorph Advanced Imaging acquisition software v.7.7.8.0. FluoZin-3-AM and LysoTracker were loaded according to the manufacturer's instructions. Briefly, FluoZin-3AM (1 mM stock solution in DMSO) was diluted to a final concentration of 3 μM in respective culture mediums. A 1 mM stock solution of LysoTracker RED DND-99 was diluted to a final concentration of 0.5 μM in respective culture mediums. Cells were loaded with the dye-containing buffer for 30 min before image collection. For time-lapse imaging of PI fluorescence (Videos S1 and S2), cells were challenged with DMEM supplemented with 10 $\mu\text{g}/\text{mL}$ PI, and images were taken at an interval of 5 or 10 min for M12 cells and MeWo cells, respectively. For MitoTracker live imaging, cells were loaded with MitoTracker and treated with ML-SAs (1h for melanocytes and MeWo cells, 30 min for M12 cells). For most inhibitor experiments, drugs were pretreated for 30 min. Images were acquired and analyzed with MetaMorph Advanced imaging acquisition software v.7.7.8.0 and ImageJ (NIH).

Electron microscopy—EM was performed at the Microscopy Core at the University of Michigan. Briefly, M12 cells were plated in the conventional TEM cell monolayer consumables (4 Thermanox 8mm coverslips and a 12-well culture plate). Cells were treated with DMSO or SA5 (3 μM) for 30 min, fixed with 2.5% glutaraldehyde in 0.1M sodium cacodylate buffer, and then processed for Epon embedding (Electron Microscopy Sciences, 14,120). Sections of 70 nm were mounted onto Formvar-coated nickel grids (Electron Microscopy Sciences, FF200-Ni) and double contrasted with 2% uranyl acetate (Electron Microscopy Sciences, 22400) for 5 min and 3% lead citrate (Electron Microscopy Sciences, 17810) for 5 min. Grids were imaged using a JEM 1400plus TEM imaging system with an AMT XR81M-B camera. Mitochondria were morphologically identified. Images were analyzed using ImageJ.

GZnP3 Zn²⁺ imaging—GZnP3 imaging was performed in HEK293 and MeWo cells that were transiently transfected with GZnP3-ML1 or GZnP3-Rab7 as described previously (Minckley et al., 2019). The fluorescence intensity at 488 nm was recorded with an EasyRatioPro system (Photon Technology International, Inc. New Jersey, USA).

QUANTIFICATION AND STATISTICAL ANALYSIS

Average data are presented as means \pm standard errors of the mean (SEMs). Statistical comparisons were made by using Student's t test or one way ANOVA. Differences were considered significant at * $p < 0.05$, ** $p < 0.01$, *** $p < 0.001$. Survival curves were

compared using the Log-rank test. All data analyses were conducted using Origin Pro 2019 or GraphPad Prism 8.0.

Supplementary Material

Refer to Web version on PubMed Central for supplementary material.

ACKNOWLEDGMENTS

We are grateful to Dr. Khalid Shah for sharing M12-FmC and MeWo-FmC cells, Dr. Jann Sarkaria for providing M12 cells, Dr. David Fisher for providing immortalized human melanocytes, and Dr. Yan Qin for the GZnP3 constructs. We thank Dr. Yanzhuang Wang for TEM image consultation. This work was supported by an NIH grant (R21-CA252428 to W.D.). Additional support was provided by an M-Cubed grant from the University of Michigan. A sponsored research grant from CalyGene Biotechnology provided interim funding for research supplies. The funders had no role in study design, data collection and analysis, decision to publish, or preparation of the manuscript.

REFERENCES

- Beyersmann D, and Haase H (2001). Functions of zinc in signaling, proliferation and differentiation of mammalian cells. *Biometals* 14, 331–341. [PubMed: 11831463]
- Blaby-Haas CE, and Merchant SS (2014). Lysosome-related organelles as mediators of metal homeostasis. *J. Biol. Chem* 289, 28129–28136. [PubMed: 25160625]
- Bos PD, Zhang XH, Nadal C, Shu W, Gomis RR, Nguyen DX, Minn AJ, van de Vijver MJ, Gerald WL, Foekens JA, and Massagué J (2009). Genes that mediate breast cancer metastasis to the brain. *Nature* 459, 1005–1009. [PubMed: 19421193]
- Cain K, Inayat-Hussain SH, Couet C, and Cohen GM (1996). A cleavage-site-directed inhibitor of interleukin-1 beta-converting enzyme-like proteases inhibits apoptosis in primary cultures of rat hepatocytes. *Biochem. J* 314, 27–32. [PubMed: 8660294]
- Chandler P, Kochupurakkal BS, Alam S, Richardson AL, Soybel DI, and Kelleher SL (2016). Subtype-specific accumulation of intracellular zinc pools is associated with the malignant phenotype in breast cancer. *Mol. Cancer* 15, 2. [PubMed: 26728511]
- Cheng X, Shen D, Samie M, and Xu H (2010). Mucopolipins: Intracellular TRPML1–3 channels. *FEBS Lett.* 584, 2013–2021. [PubMed: 20074572]
- Cuajungco MP, Basilio LC, Silva J, Hart T, Tringali J, Chen CC, Biel M, and Grimm C (2014). Cellular zinc levels are modulated by TRPML1-TMEM163 interaction. *Traffic* 15, 1247–1265. [PubMed: 25130899]
- Degterev A, Huang Z, Boyce M, Li Y, Jagtap P, Mizushima N, Cuny GD, Mitchison TJ, Moskowitz MA, and Yuan J (2005). Chemical inhibitor of nonapoptotic cell death with therapeutic potential for ischemic brain injury. *Nat. Chem. Biol* 1, 112–119. [PubMed: 16408008]
- Devinney MJ 2nd, Reynolds IJ, and Dineley KE (2005). Simultaneous detection of intracellular free calcium and zinc using fura-2FF and FluoZin-3. *Cell Calcium* 37, 225–232. [PubMed: 15670869]
- Dineley KE, Votyakova TV, and Reynolds IJ (2003). Zinc inhibition of cellular energy production: implications for mitochondria and neurodegeneration. *J. Neurochem* 85, 563–570. [PubMed: 12694382]
- Dixon SJ, Lemberg KM, Lamprecht MR, Skouta R, Zaitsev EM, Gleason CE, Patel DN, Bauer AJ, Cantley AM, Yang WS, et al. (2012). Ferroptosis: an iron-dependent form of nonapoptotic cell death. *Cell* 149, 1060–1072. [PubMed: 22632970]
- Dong XP, Cheng X, Mills E, Delling M, Wang F, Kurz T, and Xu H (2008). The type IV mucopolipidosis-associated protein TRPML1 is an endolysosomal iron release channel. *Nature* 455, 992–996. [PubMed: 18794901]
- Du W, Seah I, Bougazzoul O, Choi G, Meeth K, Bosenberg MW, Wakimoto H, Fisher D, and Shah K (2017). Stem cell-released oncolytic herpes simplex virus has therapeutic efficacy in brain metastatic melanomas. *Proc. Natl. Acad. Sci. USA* 114, E6157–E6165. [PubMed: 28710334]

- Eichelsdoerfer JL, Evans JA, Slaugenhaupt SA, and Cuajungco MP (2010). Zinc dyshomeostasis is linked with the loss of mucopolipidosis IV-associated TRPML1 ion channel. *J. Biol. Chem* 285, 34304–34308. [PubMed: 20864526]
- Finicle BT, Jayashankar V, and Edinger AL (2018). Nutrient scavenging in cancer. *Nat. Rev. Cancer* 18, 619–633. [PubMed: 30097614]
- Gao W, Pu Y, Luo KQ, and Chang DC (2001). Temporal relationship between cytochrome c release and mitochondrial swelling during UV-induced apoptosis in living HeLa cells. *J. Cell Sci* 114, 2855–2862. [PubMed: 11683418]
- Gao M, Yi J, Zhu J, Minikes AM, Monian P, Thompson CB, and Jiang X (2019). Role of Mitochondria in Ferroptosis. *Mol. Cell* 73, 354–363.e3. [PubMed: 30581146]
- Garrity AG, Wang W, Collier CM, Levey SA, Gao Q, and Xu H (2016). The endoplasmic reticulum, not the pH gradient, drives calcium refilling of lysosomes. *eLife* 5, e15887. [PubMed: 27213518]
- Haase H, and Beyersmann D (1999). Uptake and intracellular distribution of labile and total Zn(II) in C6 rat glioma cells investigated with fluorescent probes and atomic absorption. *Biometals* 12, 247–254. [PubMed: 10581689]
- Hämälistö S, and Jäättelä M (2016). Lysosomes in cancer—living on the edge (of the cell). *Curr. Opin. Cell Biol* 39, 69–76. [PubMed: 26921697]
- Jensen SS, Aaberg-Jessen C, Christensen KG, and Kristensen B (2013). Expression of the lysosomal-associated membrane protein-1 (LAMP-1) in astrocytomas. *Int. J. Clin. Exp. Pathol* 6, 1294–1305. [PubMed: 23826410]
- Jung J, Cho KJ, Naji AK, Clemons KN, Wong CO, Villanueva M, Gregory S, Karagas NE, Tan L, Liang H, et al. (2019). HRAS-driven cancer cells are vulnerable to TRPML1 inhibition. *EMBO Rep.* 20, e46685. [PubMed: 30787043]
- Kallunki T, Olsen OD, and Jäättelä M (2013). Cancer-associated lysosomal changes: friends or foes? *Oncogene* 32, 1995–2004. [PubMed: 22777359]
- Katheder NS, Khezri R, O'Farrell F, Schultz SW, Jain A, Rahman MM, Schink KO, Theodossiou TA, Johansen T, Juhász G, et al. (2017). Micro-environmental autophagy promotes tumour growth. *Nature* 541, 417–420. [PubMed: 28077876]
- Koh JY, Suh SW, Gwag BJ, He YY, Hsu CY, and Choi DW (1996). The role of zinc in selective neuronal death after transient global cerebral ischemia. *Science* 272, 1013–1016. [PubMed: 8638123]
- Kroemer G, and Jäättelä M (2005). Lysosomes and autophagy in cell death control. *Nat. Rev. Cancer* 5, 886–897. [PubMed: 16239905]
- Kroemer G, Galluzzi L, Vandenabeele P, Abrams J, Alnemri ES, Baehrecke EH, Blagosklonny MV, El-Deiry WS, Golstein P, Green DR, et al. ; Nomenclature Committee on Cell Death 2009 (2009). Classification of cell death: recommendations of the Nomenclature Committee on Cell Death 2009. *Cell Death Differ.* 16, 3–11. [PubMed: 18846107]
- Kukic I, Lee JK, Coblenz J, Kelleher SL, and Kiselyov K (2013). Zinc-dependent lysosomal enlargement in TRPML1-deficient cells involves MTF-1 transcription factor and ZnT4 (Slc30a4) transporter. *Biochem. J* 451, 155–163. [PubMed: 23368743]
- Lawrence RE, and Zoncu R (2019). The lysosome as a cellular centre for signalling, metabolism and quality control. *Nat. Cell Biol* 21, 133–142. [PubMed: 30602725]
- Li X, Rydzewski N, Hider A, Zhang X, Yang J, Wang W, Gao Q, Cheng X, and Xu H (2016). A molecular mechanism to regulate lysosome motility for lysosome positioning and tubulation. *Nat. Cell Biol* 18, 404–417. [PubMed: 26950892]
- Li P, Gu M, and Xu H (2019). Lysosomal Ion Channels as Decoders of Cellular Signals. *Trends Biochem. Sci* 44, 110–124. [PubMed: 30424907]
- Maret W, Jacob C, Vallee BL, and Fischer EH (1999). Inhibitory sites in enzymes: zinc removal and reactivation by thionein. *Proc. Natl. Acad. Sci. USA* 96, 1936–1940. [PubMed: 10051573]
- McAfee Q, Zhang Z, Samanta A, Levi SM, Ma XH, Piao S, Lynch JP, Uehara T, Sepulveda AR, Davis LE, et al. (2012). Autophagy inhibitor Lys05 has single-agent antitumor activity and reproduces the phenotype of a genetic autophagy deficiency. *Proc. Natl. Acad. Sci. USA* 109, 8253–8258. [PubMed: 22566612]

- Medina DL, Di Paola S, Peluso I, Armani A, De Stefani D, Venditti R, Montefusco S, Scotto-Rosato A, Prezioso C, Forrester A, et al. (2015). Lysosomal calcium signalling regulates autophagy through calcineurin and TFEB. *Nat. Cell Biol* 17, 288–299. [PubMed: 25720963]
- Minckley TF, Zhang C, Fudge DH, Dischler AM, LeJeune KD, Xu H, and Qin Y (2019). Sub-nanomolar sensitive GZnP3 reveals TRPML1-mediated neuronal Zn²⁺ signals. *Nat. Commun* 10, 4806. [PubMed: 31641116]
- Napolitano G, and Ballabio A (2016). TFEB at a glance. *J. Cell Sci* 129, 2475–2481. [PubMed: 27252382]
- Narayana A, Mathew M, Tam M, Kannan R, Madden KM, Golfinos JG, Parker EC, Ott PA, and Pavlick AC (2013). Vemurafenib and radiation therapy in melanoma brain metastases. *J. Neurooncol* 113, 411–416. [PubMed: 23579338]
- Orrenius S, and Nicotera P (1994). The calcium ion and cell death. *J. Neural Transm. Suppl* 43, 1–11. [PubMed: 7884392]
- Palmiter RD, Cole TB, and Findley SD (1996). ZnT-2, a mammalian protein that confers resistance to zinc by facilitating vesicular sequestration. *EMBO J.* 15, 1784–1791. [PubMed: 8617223]
- Pavlova NN, and Thompson CB (2016). The Emerging Hallmarks of Cancer Metabolism. *Cell Metab.* 23, 27–47. [PubMed: 26771115]
- Peng W, Wong YC, and Krainc D (2020). Mitochondria-lysosome contacts regulate mitochondrial Ca²⁺ dynamics via lysosomal TRPML1. *Proc. Natl. Acad. Sci. USA* 117, 19266–19275. [PubMed: 32703809]
- Pérez-Sayáns M, Somoza-Martín JM, Barros-Angueira F, Rey JM, and García-García A (2009). V-ATPase inhibitors and implication in cancer treatment. *Cancer Treat. Rev* 35, 707–713. [PubMed: 19758758]
- Petersen NH, Olsen OD, Groth-Pedersen L, Ellegaard AM, Bilgin M, Redmer S, Ostensfeld MS, Ulanet D, Dovmark TH, Lønborg A, et al. (2013). Transformation-associated changes in sphingolipid metabolism sensitize cells to lysosomal cell death induced by inhibitors of acid sphingomyelinase. *Cancer Cell* 24, 379–393. [PubMed: 24029234]
- Piao S, and Amaravadi RK (2016). Targeting the lysosome in cancer. *Ann. N Y Acad. Sci* 1371, 45–54. [PubMed: 26599426]
- Petrobono S, Anichini G, Sala C, Manetti F, Almada LL, Pepe S, Carr RM, Paradise BD, Sarkaria JN, Davila JI, et al. (2020). ST3GAL1 is a target of the SOX2-GLI1 transcriptional complex and promotes melanoma metastasis through AXL. *Nat. Commun* 10.1038/s41467-020-19575-2.
- Radford RJ, and Lippard SJ (2013). Chelators for investigating zinc metal-loneurochemistry. *Curr. Opin. Chem. Biol* 17, 129–136. [PubMed: 23478014]
- Saftig P, and Klumperman J (2009). Lysosome biogenesis and lysosomal membrane proteins: trafficking meets function. *Nat. Rev. Mol. Cell Biol* 10, 623–635. [PubMed: 19672277]
- Sahoo N, Gu M, Zhang X, Raval N, Yang J, Bekier M, Calvo R, Patnaik S, Wang W, King G, et al. (2017). Gastric Acid Secretion from Parietal Cells Is Mediated by a Ca²⁺ Efflux Channel in the Tubulovesicle. *Dev. Cell* 41, 262–273.e6. [PubMed: 28486130]
- Samie M, Wang X, Zhang X, Goschka A, Li X, Cheng X, Gregg E, Azar M, Zhuo Y, Garrity AG, et al. (2013). A TRP channel in the lysosome regulates large particle phagocytosis via focal exocytosis. *Dev. Cell* 26, 511–524. [PubMed: 23993788]
- Schmiege P, Fine M, Blobel G, and Li X (2017). Human TRPML1 channel structures in open and closed conformations. *Nature* 550, 366–370. [PubMed: 29019983]
- Schmiege P, Fine M, and Li X (2021). Atomic insights into ML-SI3 mediated human TRPML1 inhibition. *Structure*, Published online June 19, 2021. 10.1016/j.str.2021.06.003.
- Serrano-Puebla A, and Boya P (2018). Lysosomal membrane permeabilization as a cell death mechanism in cancer cells. *Biochem. Soc. Trans* 46, 207–215. [PubMed: 29472365]
- Shekoufeh Almasi, K. BE, Yeast Ryan, E., Emrich Scott, M., Trebak Mohamed, and Hiani Yassine El(2020). The lysosomal TRPML1 channel promotes breast cancer survival by supporting mitochondrial function and cellular metabolism. *bioRxiv*. 10.1101/20200904283242.
- Sheline CT, Behrens MM, and Choi DW (2000). Zinc-induced cortical neuronal death: contribution of energy failure attributable to loss of NAD(+) and inhibition of glycolysis. *J. Neurosci* 20, 3139–3146. [PubMed: 10777777]

- Shen D, Wang X, Li X, Zhang X, Yao Z, Dibble S, Dong XP, Yu T, Lieberman AP, Showalter HD, and Xu H (2012). Lipid storage disorders block lysosomal trafficking by inhibiting a TRP channel and lysosomal calcium release. *Nat. Commun* 3, 731. [PubMed: 22415822]
- Shiku H, Takahashi T, and Oettgen HF (1976). Cell surface antigens of human malignant melanoma. II. Serological typing with immune adherence assays and definition of two new surface antigens. *J. Exp. Med* 144, 873–881. [PubMed: 978138]
- Tardy C, Codogno P, Autefage H, Levade T, and Andrieu-Abadie N (2006). Lysosomes and lysosomal proteins in cancer cell death (new players of an old struggle). *Biochim. Biophys. Acta* 1765, 101–125. [PubMed: 16412578]
- Tasdemir E, Galluzzi L, Maiuri MC, Criollo A, Vitale I, Hangen E, Modjtahedi N, and Kroemer G (2008). Methods for assessing autophagy and autophagic cell death. *Methods Mol. Biol* 445, 29–76. [PubMed: 18425442]
- Venugopal B, Browning MF, Curcio-Morelli C, Varro A, Michaud N, Nanthakumar N, Walkley SU, Pickel J, and Slaughter SA (2007). Neurologic, gastric, and ophthalmologic pathologies in a murine model of mucopolidosis type IV. *Am. J. Hum. Genet* 81, 1070–1083. [PubMed: 17924347]
- WebLink (2019). <https://www.proteinatlas.org/ENSG00000090674-MCOLN1/pathology>.
- Welsh SJ, Rizos H, Scolyer RA, and Long GV (2016). Resistance to combination BRAF and MEK inhibition in metastatic melanoma: Where to next? *Eur. J. Cancer* 62, 76–85. [PubMed: 27232329]
- Xie S, Price JE, Luca M, Jean D, Ronai Z, and Bar-Eli M (1997). Dominant-negative CREB inhibits tumor growth and metastasis of human melanoma cells. *Oncogene* 15, 2069–2075. [PubMed: 9366524]
- Xu M, Almasi S, Yang Y, Yan C, Sterea AM, Rizvi Syeda AK, Shen B, Richard Derek C, Huang P, Gujar S, et al. (2019). The lysosomal TRPML1 channel regulates triple negative breast cancer development by promoting mTORC1 and purinergic signaling pathways. *Cell Calcium* 79, 80–88. [PubMed: 30889511]
- Yang Y, Kawataki T, Fukui K, and Koike T (2007). Cellular Zn²⁺ chelators cause “dying-back” neurite degeneration associated with energy impairment. *J. Neurosci. Res* 85, 2844–2855. [PubMed: 17628505]
- Yu L, Zhang X, Yang Y, Li D, Tang K, Zhao Z, He W, Wang C, Sahoo N, Converso-Baran K, et al. (2020). Small-molecule activation of lysosomal TRP channels ameliorates Duchenne muscular dystrophy in mouse models. *Sci. Adv* 6, eaaz2736. [PubMed: 32128386]
- Zhang X, Cheng X, Yu L, Yang J, Calvo R, Patnaik S, Hu X, Gao Q, Yang M, Lawas M, et al. (2016). MCOLN1 is a ROS sensor in lysosomes that regulates autophagy. *Nat. Commun* 7, 12109. [PubMed: 27357649]
- Zhang X, Chen W, Gao Q, Yang J, Yan X, Zhao H, Su L, Yang M, Gao C, Yao Y, et al. (2019). Rapamycin directly activates lysosomal mucolipin TRP channels independent of mTOR. *PLoS Biol.* 17, e3000252. [PubMed: 31112550]

Highlights

- TRPML1 is dramatically upregulated in metastatic melanoma cells
- Activation of TRPML1, instead of inhibition, induces selective melanoma cell death
- TRPML-specific synthetic agonists (ML-SAs) trigger a distinctive form of cell death
- ML-SAs exhibit potent *in vivo* therapeutic efficacy in advanced melanoma mouse models

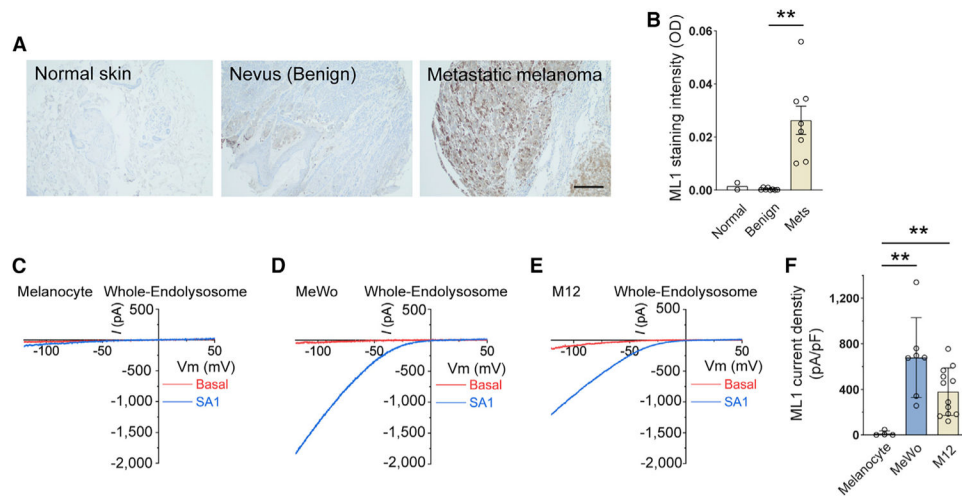


Figure 1. Lysosomal ML1 is upregulated in metastatic melanoma cells

(A) Representative images of human tissue sections from normal skin, nevus (benign tumor), and metastatic melanoma immunostained with an anti-ML1 antibody (brown DAB staining). Scale bar, 200 μ m.

(B) Quantification of ML1 immunostaining from normal skin tissue (Normal; $n = 2$ cases), nevus (Benign; $n = 8$ cases), and metastatic melanoma (Mets; $n = 8$ cases). Each open circle represents one case.

(C–E) Whole-endolysosome ML1 currents (I_{ML1}) were activated by ML-SA1 (20 μ M), a synthetic agonist of ML1, in an immortalized human melanocyte (C), a MeWo cell (D), and a M12 cell (E). Currents were recorded with a ramp voltage protocol from -120 to $+120$ mV (only partial voltage ranges are shown). Pipette (luminal) solution was a standard external (Tyrode's) solution adjusted to pH 4.6 to mimic the acidic environment of the lysosome lumen. Bath (cytoplasmic) solution was a K^+ -based solution (140 mM K-gluconate). Note that the inward currents indicate cations flowing out of endolysosomes.

(F) Mean current densities of whole-endolysosome I_{ML1} in normal melanocytes ($n = 4$), MeWo cells ($n = 7$), and M12 cells ($n = 12$). Each open circle represents one endolysosome/patch/cell; average data are presented as mean \pm SEM; ** $p < 0.01$.

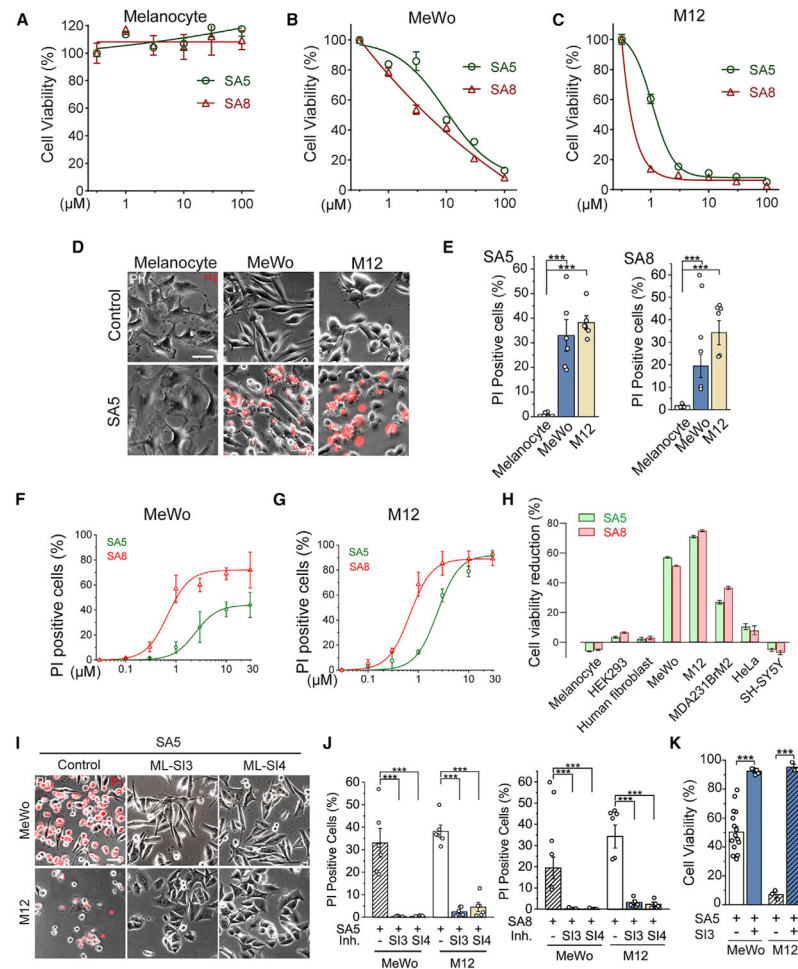


Figure 2. Selective cytotoxic effects of ML-SAs on metastatic melanoma cells

(A–C) Dose-dependent effects of SA5 and SA8 on cell viabilities of normal melanocytes, MeWo, and M12 cells, which were measured using the CellTiter-Glo ATP assay 24 h after drug treatment. The average data represent mean \pm SEM from three independent experiments, each with triplicates.

(D) PI staining of MeWo and M12 cells in the presence or absence of SA5 (3 μ M). Normal melanocytes and MeWo cells were drug treated for 6 h, and M12 cells were drug treated for 3 h. Overlay phase contrast (Ph) images are also shown. Scale bar, 25 μ m.

(E) The percentage of PI-positive cells in the presence of SA5 (3 μ M, the left panels), as in (D), and SA8 (1 μ M, right panels). Each open circle represents the average data from one batch of cells for each independent experiment.

(F and G) Dose-dependent effects of SA5/8 on the percentages of PI-positive MeWo (6 h) and M12 (3 h) cells.

(H) The effects of ML-SAs (3 μ M SA5 or 1 μ M SA8 for 12 h) on the cell viabilities of multiple cell types (n = 3 independent experiments).

(I) Overlay phase contrast and fluorescence images of PI-stained SA5 (3 μ M)-treated MeWo (for 6 h) and M12 (for 3 h) cells in the presence or absence of ML-SIs (SI3 and SI4, 20 μ M). Scale bar, 25 μ m.

(J) The percentage of PI-positive cells under indicated conditions. Each open circle represents one batch of cells. Note that the control (Ctrl) groups of MeWo and M12 treated with SA5 or SA8 are re-plotted from (E), as they were from the same experiments.

(K) Cell viability analysis of MeWo and M12 cells treated with SA5 in the presence or absence of ML-SI3 (12 h). In all panels, average data are presented as mean \pm SEM; *** $p < 0.001$.

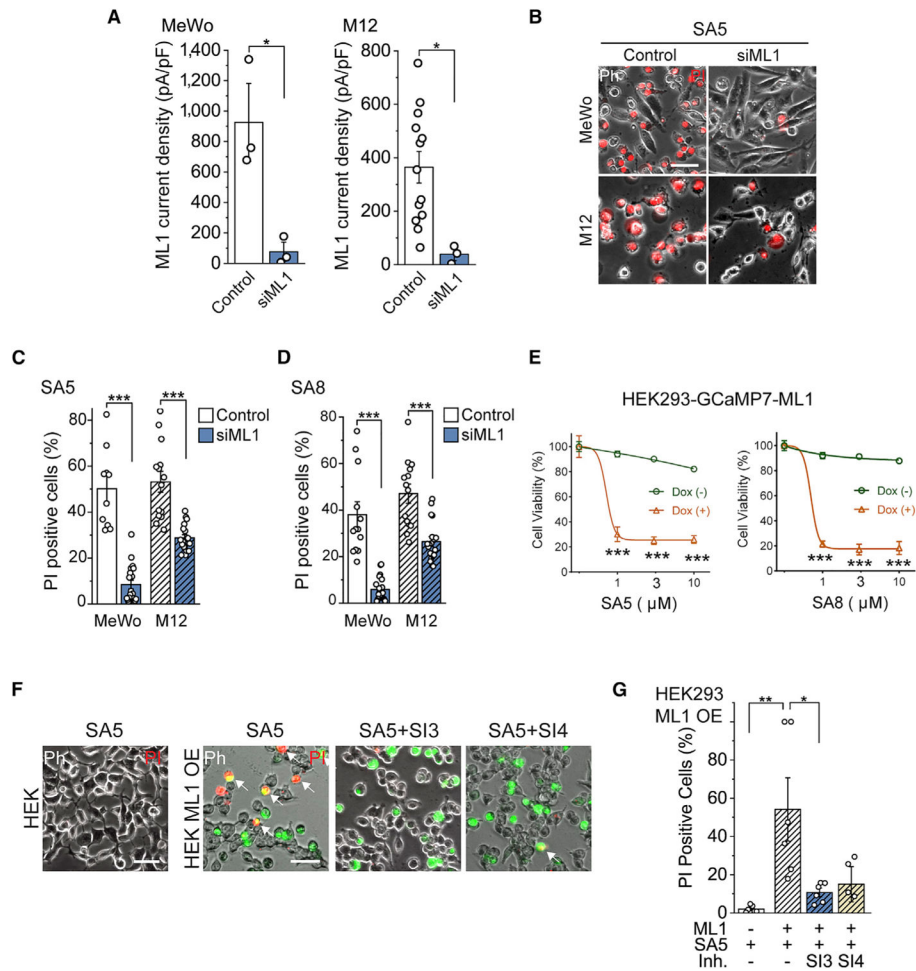


Figure 3. ML1 is required for ML-SA-induced cell death

(A) Mean current densities of whole-endolysosome I_{ML1} in Ctrl or ML1-specific siRNA (siML1)-transfected MeWo and M12 cells. Each open circle represents one endolysosome/cell/patch.

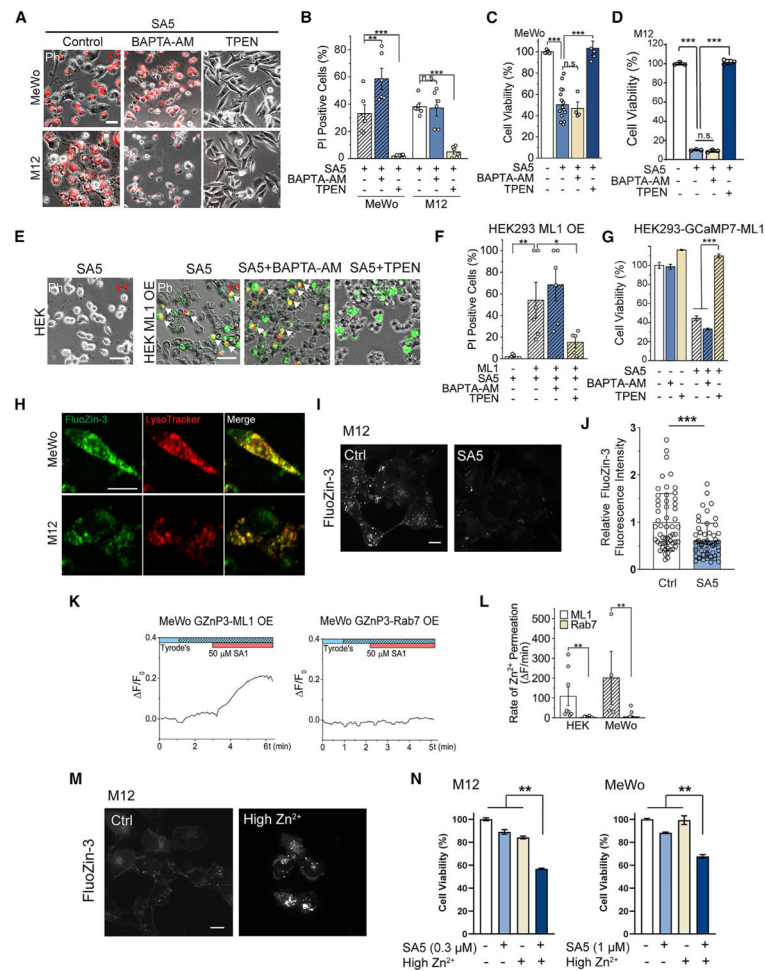
(B) PI-staining of Ctrl or siML1-transfected MeWo and M12 cells in the presence of SA5 (3 μ M) for 3 to 6 h. The overlay phase contrast and PI images are also shown. Scale bar, 25 μ m.

(C and D) The percentages of PI-positive control or siML1-transfected cells treated with SA5 (C) or SA8 (D).

(E) Dose-dependent effects of SA5 (left panel) and SA8 (right panel) (12 h) on cell viability of Tet-On HEK293-GCaMP7-ML1 cells with (Dox⁺) or without doxycycline (Dox⁻) induction.

(F) PI staining of HEK293 and HEK293 transiently expressing EGFP-ML1 (HEK ML1 OE) cells under indicated drug treatments for 6 h. The overlay phase contrast images are shown together with the green (EGFP-ML1) and red (PI staining) fluorescence channels. White arrows point to the EGFP-positive cells (i.e., with successful expression of EGFP-ML1) that are also PI positive. Scale bar, 25 μ m.

(G) The percentages of PI-positive ML1-overexpressing HEK293 cells (HEK293 ML1 OE) upon SA5 treatment (3 μ M) in the presence and absence of ML-SI3/4 (20 μ M), as shown in (F). Average data are presented as mean \pm SEM; * p < 0.05, ** p < 0.01, *** p < 0.001.



(H) Fluorescence images of MeWo and M12 cells stained with both FluoZin-3 (–AM) and LysoTracker. Scale bar, 5 μ m.

(I) FluoZin-3 staining of M12 cells treated with DMSO (Ctrl) and SA5 (3 μ M) for 30 min. Scale bar, 5 μ m.

(J) Statistical analysis of relative FluoZin-3 intensity in control (n = 55 cells) and SA5 treatment (n = 56 cells) experiments, as shown in (I).

(K) The effects of SA1 on GZnP3 imaging of MeWo cells transfected with GZnP3-ML1 or GZnP3-Rab7 in the presence of 100 μ M Zn²⁺.

(L) The rates of SA1-induced Zn²⁺ flux in GZnP3 (ML1- or Rab7-) transfected HEK293 and MeWo cells (calculated as in K).

(M) FluoZin-3 imaging of M12 cells that were incubated with a normal (Ctrl) or high Zn²⁺ (100 μ M) growth medium for 12 h.

(N) Cell viability analysis of M12 (left panel) and MeWo (right panel) cells that were treated with indicated chemicals for 12 h. All data are mean \pm SEM; *p < 0.05, **p < 0.01, ***p < 0.001.

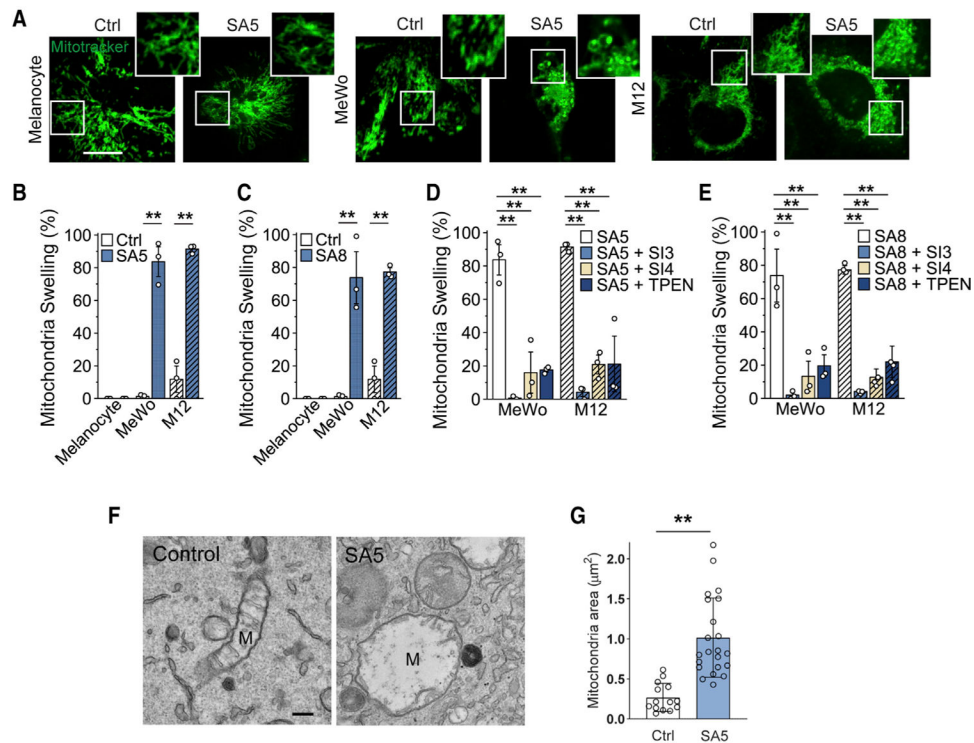


Figure 5. ML-SAs cause mitochondrial swelling in metastatic melanoma cells

(A) Live imaging of MitoTracker-loaded normal melanocytes (left panels, 60 min), MeWo (middle panels, 60 min), and M12 (right panels, 30 min) cells under DMSO (Ctrl) or SA5 (3 μM) treatment. Scale bar, 10 μm .

(B and C) Statistical analysis of mitochondrial swelling in melanocytes, MeWo, and M12 cells that were treated with SA5 (3 μM) or SA8 (1 μM) for 30 or 60 min. Each open circle represents the average result from one batch of cells.

(D and E) The effects of ML-SIs and TPEN on mitochondrial swelling in SA5 (D) or SA8 (E)-treated MeWo and M12 cells. Note that the control groups of MeWo and M12 treated with SA5 or SA8 are re-plotted from (B) and (C), as they were from the same experiments.

(F) Representative transmission electron microscopy (TEM) images of M12 cells that were treated with DMSO (Ctrl) or SA5 (3 μM) for 30 min. M, mitochondria. Scale bar, 200 nm.

(G) Statistical analysis of mitochondrial size in control ($n = 14$ mitochondria from 3 cells) and SA5-treated cells ($n = 22$ mitochondria from 5 cells). All data are mean \pm SEM; ** $p < 0.01$.

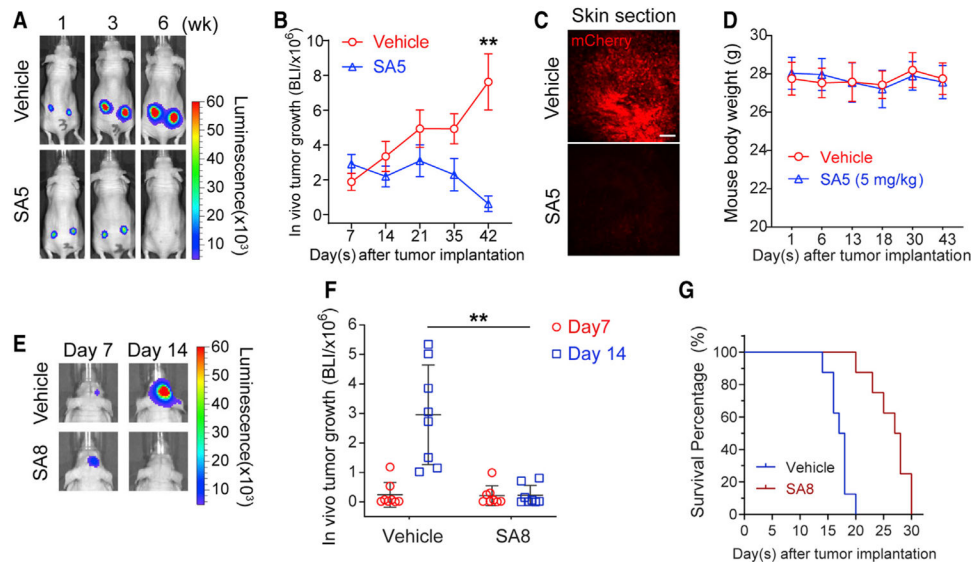


Figure 6. *In vivo* efficacy of ML-SAs on suppressing tumor growth in advanced melanoma mouse models

(A) Representative bioluminescence images (BLI) of MeWo-FmC-tumor bearing mice treated with vehicle or SA5 (5 mg/kg mouse weight).

(B) Statistical analysis of *in vivo* MeWo-FmC tumor growth in vehicle versus SA5-treated mice (n = 5 mice per group).

(C) Representative mCherry fluorescence imaging of MeWo-FmC tumor cells (red) in skin sections from vesicle or SA5-treated tumor bearing mice (sample collection at day 42). Scale bar, 50 μ m.

(D) The effects of drug treatment on mouse body weight.

(E) Representative bioluminescence images of M12-FmC-tumor bearing mice treated with vehicle or SA8 on day 7 after tumor implantation (before drug administration at day 8) and day 14 (1 week after drug administration); single intracranial injection with vehicle (DMSO) or SA8 (10 mM/5 μ l) was conducted at day 8.

(F) Statistical analysis of *in vivo* M12-FmC brain tumor growth in vehicle versus SA8-treated mice (n = 8 mice per group). Each open circle/square represents one mouse.

(G) Kaplan-Meier survival analysis of M12-FmC tumor-bearing mice treated with vehicle or SA8 (n = 8 mice per group). Log-rank test, $p < 0.001$. For all other panels, data are mean \pm SEM; ** $p < 0.01$.

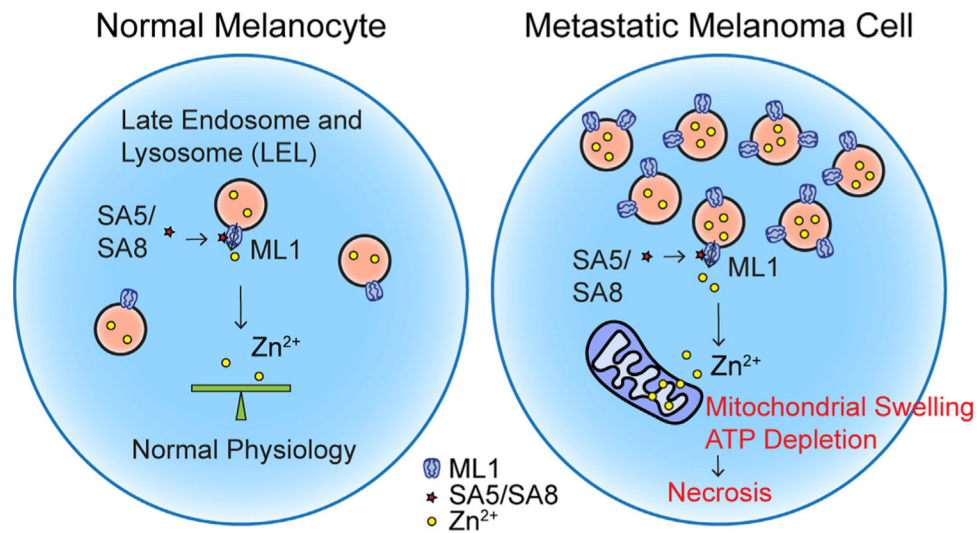


Figure 7. Activation of upregulated ML1 channels in the lysosomal Zn²⁺ stores in duces Zn²⁺ release and selective necrotic cell death in metastatic melanoma cells

Lysosome number and machinery, including lysosomal ML1 channels, are maladaptively upregulated in metastatic melanoma cells compared with normal melanocytes. In metastatic melanoma cells, but not in normal melanocytes, ML-SA administration results in excessive ML1 activation and lysosomal Zn²⁺ release, causing mitochondrial swelling/damage, cellular ATP depletion, and necrotic cell death (which we termed “*Lysozincrosis*”).

KEY RESOURCES TABLE

REAGENT OR RESOURCE	SOURCE	IDENTIFIER
Antibodies		
Rabbit anti-TRPML1 (Mucolipin 1) Antibody	Alomone Labs	Cat# ACC-081; RRID:AB_10915894
Mouse anti-human LAMP1 (H4A3) antibody	DSHB	Cat# h4a3; RRID: AB_2296838
Mouse Anti-beta-Actin Antibody (AC-74)	Sigma-Aldrich	Cat# A5316; RRID: AB_476743
Goat anti-Rabbit IgG (H+L) Secondary Antibody, HRP	Fisher Scientific	Cat# 31460; RRID: AB_228341
Goat anti-Mouse IgG (H+L) Secondary Antibody, HRP	Fisher Scientific	Cat# 31430; RRID: AB_228307
Chemicals, peptides, and recombinant proteins		
ML-SAs (SA1, SA5, SA8)	Shen et al., 2012; Sahoo et al., 2017; Yu et al., 2020; This paper; National Institutes of Health (NIH)/National Center for Advancing Translational Sciences (NCATS) Chemical Genomics Center & CalyGene Biotechnology Inc.	N.A.
ML-SIs (SI3, SI4)	Sahoo et al., 2017; National Institutes of Health (NIH)/National Center for Advancing Translational Sciences (NCATS) Chemical Genomics Center	N.A.
K-Gluconate	Sigma-Aldrich	P1847; CAS: 299-27-4
NaCl	Sigma-Aldrich	S9888; CAS: 7647-14-5
EGTA	Sigma-Aldrich	E4378; CAS: 67-42-5
MgCl ₂	Sigma-Aldrich	208337; CAS: 7786-30-3
CaCl ₂	Sigma-Aldrich	C8106; CAS: 10035-04-8
MgCl ₂	Sigma-Aldrich	1374248; CAS: 7791-18-6
ZnCl ₂	Sigma-Aldrich	208086; CAS: 7646-85-7
Glucose	Sigma-Aldrich	G6152; CAS: 50-99-7
HEPES	Sigma-Aldrich	H3375; CAS: 7365-45-9
KOH	Sigma-Aldrich	P250-500; CAS: 1310-58-3
NaCl	Sigma-Aldrich	S9888; CAS: 10035-04-8
KCl	Sigma-Aldrich	P9541; CAS: 7447-40-7
MES	Sigma-Aldrich	M8250; CAS: 1266615-59-1
NaOH	Fisher Scientific	S318-500; CAS: 1310-73-2
Propidium iodide	Sigma-Aldrich	P4864
Ethanol	Decon laboratories inc.	2701; CAS: 64-17-5
Hydrogen peroxide	Sigma-Aldrich	H1009; CAS: 7722-84-1
Triton X-100	Sigma-Aldrich	T8787; CAS: 9002-93-1
NaF	Sigma-Aldrich	S7920; CAS: 7681-49-4
Na-orthovanadate	Sigma-Aldrich	S6508; CAS: 13721-39-6
Dimethyl sulfoxide (DMSO)	Sigma-Aldrich	D2650; CAS: 67-68-5
Bovine Serum Albumin (BSA)	Sigma-Aldrich	A3059; CAS: 9048-46-8
Paraformaldehyde (PFA) 4% in PBS	Fisher Scientific	J19943-K2
Phosphate-buffered saline (PBS)	Fisher Scientific	10010023
HBSS, calcium, magnesium, no phenol red	Fisher Scientific	14025092
RIPA	Boston Bioproducts	BP-115

REAGENT OR RESOURCE	SOURCE	IDENTIFIER
Protease inhibitor cocktail	Sigma Aldrich	P8340
Phosphatase inhibitor cocktail I	Sigma Aldrich	P0044
LDS sample buffer (4x)	Invitrogen	NP0007
Pierce BCA Protein Assay	Invitrogen	23227
PVDF membrane	Millipore	IPFL00010
Tween-20	Fisher Scientific	BP337-100; CAS: 9005-64-5
SuperSignal West Atto Ultimate Sensitivity Substrate	Fisher Scientific	A38555
LysoTracker™ Red DND-99	Invitrogen	L7528
MitoTracker Green FM	Invitrogen	M7514
FluoZin-3, AM	Fisher Scientific	F24195
BAPTA, AM	Fisher Scientific	B6769
Tetramethylrhodamine, Methyl Ester, Perchlorate (TMRM)	Fisher Scientific	T668
N,N,N',N'-tetrakis(2-pyridinylmethyl)-1,2-ethanediamine (TPEN)	Cayman Chemical	13340; CAS: 16858-02-9
Deferoxamine (Radford and Lippard)	Cayman Chemical	14595; CAS: 138-14-7
Chloroquine	Cayman Chemical	30708; CAS: 50-63-5
z-VAD-FMK	Cayman Chemical	14467; CAS: 161401-82-7
Bafilomycin-A1	Cayman Chemical	11038; CAS: 88899-55-2
Doxycycline	Sigma-Aldrich	D9891; CAS: 24390-14-5
1,10-Phenanthroline (hydrate)	Cayman Chemical	28951; CAS: 5144-89-8
Necrostatin-1	Cayman Chemical	11658; CAS: 4311-88-0
EGTA, AM	Cayman Chemical	20401; CAS: 99590-86-0
Doxorubicin	Cayman Chemical	15007; CAS: 25316-40-9
Zinc Pyrithione	Cayman Chemical	29154; CAS: 13463-41-7
Lipofectamine 2000	Invitrogen	11668-027
DMEM medium without phenol red	GIBCO	21063029
DMEM, high glucose	GIBCO	11965092
DMEM/F-12	GIBCO	11320033
Ham's F-10 Nutrient Mix	Fisher Scientific	11550043
Minimum Essential Media	Fisher Scientific	11095080
Trypsin-EDTA (0.05%), phenol red	GIBCO	25300054
Fetal bovine serum (FBS)	Gemini Bio-Products	100-106
Antibiotic-Antimycotic	GIBCO	15240062
Poly-D-lysine solution	Millipore	A-003-E
Poly-L-lysine hydrobromide	Sigma-Aldrich	P1399; CAS: 25988-63-0
Vacuolin-1	Sigma-Aldrich	673000; CAS: 351986-85-1
Ionomycin	Sigma-Aldrich	I9657; CAS: 56092-81-0
Tissue-Tek® O.C.T. (Optimal Cutting Temperature) compound	Sakura Finetek	4583
Polyethylene glycol (PEG) 300	Sigma-Aldrich	1546423; CAS: 25322-68-3
XenoLight D-Luciferin - K ⁺ Salt Bioluminescent Substrate	PerkinElmer	122799
Critical commercial assays		

REAGENT OR RESOURCE	SOURCE	IDENTIFIER
CellTiter-Glo® Luminescent Cell Viability Assay	Promega	G7571
E.Z.N.A.® Total RNA Kit I	Omega Bio-tek	R6834-01
SuperScript III One-Step RT-PCR System	Fisher Scientific	12574026
PowerUp SYBR Green Master Mix	Fisher Scientific	A25741
Q5® High-Fidelity DNA Polymerase	New England Biolabs	M0491S
GoTaq™ master mixes	Promega	M7122
MycAlert™ Mycoplasma Detection Kit	Lonza	LT07-318
Experimental models: Cell lines		
pMEL/NRAS (Q61R) immortalized human melanocyte	A gift from Dr. D. Fisher, MGH	N.A.
Human MeWo cells	ATCC	HTB-65
Human M12 cells	A gift from Dr. J. Sarkaria, Mayo Clinic; Du et al., 2017	N.A.
Human MDA231BrM2a cells	A gift from Dr. J. Massague, Memorial Sloan Cancer Center Bos et al., 2009	N.A.
Human skin fibroblast cells	Obtained from the Coriell Institute for Medical Research	clone GM05659
Human: HEK293 cells	ATCC	CRL-1573
Human: HeLa cells	ATCC	CCL-2
Human SH-SY5Y cells	ATCC	CRL-2266
TFEB-GFP Stable HeLa cells	Zhang et al., 2016; Zhang et al., 2019	N.A.
Human HEK293-GCaMP7-ML1 cells	Zhang et al., 2019	N.A.
Human M12-FmC cells	Du et al., 2017	N.A.
Human MeWo-FmC cells	Du et al., 2017	N.A.
Experimental models: Organisms/strains		
Human paraffin-embedded tissue array (Tissue Microarray, TMA)	US Biomax	ME1004
Athymic Nude Mouse	Charles River Laboratories	490 CrI:NU(NCr)-Foxn1 ^{nu}
Oligonucleotides		
<i>GAPDH</i> , forward primer	5'-tgcaccaccaactgcttagc-3'	N.A.
<i>GAPDH</i> , reverse primer	5'-ggcatggactgtggtcatgag-3'	N.A.
<i>MCOLN1</i> , forward primer	5'-gagtgggtgcgacaagtcttc-3'	N.A.
<i>MCOLN1</i> , reverse primer	5'-tgttctctcccgaatgac-3'	N.A.
Stealth siRNA human <i>TFEB</i>	Fisher Scientific	HSS111868
MISSION® esiRNA targeting human <i>MCOLN1</i>	Sigma-Aldrich	EHU062561
Recombinant DNA		
GZnP3-ML1	A gift from Dr. Yan Qin, Denver University; Minckley et al., 2019	N.A.
GZnP3-Rab7	A gift from Dr. Yan Qin, Denver University; Minckley et al., 2019	N.A.
EGFP-ML1	Shen et al., 2012	N.A.
ML1-L ¹⁵ L/AA-L ⁵⁷⁷ L/AA (abbreviated as ML1-4A)	Shen et al., 2012	N.A.
Software and algorithms		
MetaMorph 7.10	Molecular Devices	https://www.moleculardevices.com/
pClamp 10.7	Molecular Devices	https://www.moleculardevices.com/

REAGENT OR RESOURCE	SOURCE	IDENTIFIER
OriginPro 2018	Originlab	https://www.originlab.com/
GraphPad Prism 8	Graphpad	https://www.graphpad.com/
Fiji/ImageJ	Fiji contributors	https://imagej.net/software/fiji

Author Manuscript

Author Manuscript

Author Manuscript

Author Manuscript